

# Adjoint Based Shape Optimization of an S-Shaped Duct with SU<sup>2</sup>

Umut Can KUCUK\*

and

Ismail H. TUNCER†

*Middle East Technical University, Aerospace Engineering, 06800 Ankara, Turkey*

In this study, an adjoint based aerodynamic shape optimization of an intake duct is performed for a set of objectives. The objectives include the minimization of total pressure loss, the minimization of total pressure loss constrained with the minimum mass flow rate and the maximization of mass flow rate. M2129 intake duct is taken as the baseline geometry. The Flow and the adjoint solutions are obtained with the open source SU<sup>2</sup> software. Optimum configurations provide a significant increase in the total pressure recovery and better distortion characteristics compared to the baseline configuration. The optimum configurations, in general, have similar characteristics in terms of streamwise area distribution and the cross sectional shapes. It is also shown that the radial pressure gradient around the first bend is minimized as a result of high diffusion rates. In addition, the minimization of the total pressure loss results in an unexpected relation between the mass flow rate and the total pressure recovery, which is discussed in detail.

## I. Introduction

Air inlets are employed to capture a sufficient amount of external flow and transport it to the relevant aerodynamic device with the highest uniformity and minimum losses. If the captured external flow is for an aircraft engine, the performance considerations of an intake play a crucial role for whole system efficiency. Accordingly, a significant amount of experimental and computational studies on engine intakes are available in the open literature. One of the most investigated air intakes by the researchers is known as M2129 intake. This intake is introduced by the AGARD Fluid Dynamics Panel Working Group 13 test case 3.<sup>1</sup> M2129 intake is a circular cross section S-shaped duct. Although S-Ducts are chosen to take advantage of their compactness and low radar cross section by many air vehicle designers, they introduced challenges due to the strong pressure gradients that exist in both radial and axial directions.

In an S-Duct, curvature of the first bend creates centrifugal forces. These forces are higher at the inner side of the bend compared to the outer side and therefore, force imbalance occurs at the first bend in radial direction. This force imbalance further leads to static pressure gradient at the first bend so that to equalize this force imbalance static pressure at the outer region increases. Moreover, because of the relatively high centrifugal forces, flow near the inner side of the bend tends to lift up through the outer side where static pressure is high. Since static pressure is high around the outer side of the bend, flow cannot lift up and returns to the low static pressure region around the inner side of the bend. This creates secondary flows and increases losses so that is the main reason why design and optimization of S-ducts is still a challenging topic. Centrifugal forces generated at the second bend of the S-ducts cannot eliminate the secondary flows generated at the first bend because, at this location flow already loses its momentum due to the entropy generation and diffusion in stream wise direction.

In this study, flow through the M2129 intake duct is investigated computationally and a discrete adjoint based aerodynamic shape optimization is performed with the open source CFD software SU<sup>2</sup>.<sup>2</sup> It is shown that the optimization process provides a significant performance increase for the M2129 inlet duct while retaining the baseline inlet entrance and AIP surfaces, and the vertical offset distance between them. In

\*PhD Candidate, Aerospace Engineering Department, e156115@metu.edu.tr

†Professor, Aerospace Engineering Department, ismail.h.tuncer@ae.metu.edu.tr

addition, an unexpected tendency observed when the total pressure loss is minimized is discussed in detail and additional constrained optimizations are carried out. Finally, the relative performance of the S-ducts obtained as a result of the optimization processes are compared with each other as well as M2129 inlet for a range of throat Mach numbers.

## II. Method

Steady state performance of an inlet depends on two main parameters. The first one simply measures the inlet losses that occur in capturing external flow and transporting it to the engine interface. This performance parameter is known as "Pressure Recovery" and it is defined as the ratio of the total pressure at the engine interface to the free stream total pressure. The engine interface is generally called the Aerodynamic Interface Plane (AIP). The second parameter measures the flow uniformity at the AIP in terms of the variations in the total pressure distribution. The total pressure uniformity on the AIP is quantified with the DC60 parameter which is the non-dimensionalized total pressure difference between the average total pressure and the minimum average total pressure selected from every possible 60° circumferential sector on the AIP. The non dimensionalization is performed with dynamic pressure at the AIP.

In this study the total pressure at the AIP is maximized using a gradient based optimization algorithm and the DC60 parameter is monitored. In other words, inlet losses are minimized and its effect on flow uniformity is investigated. The baseline inlet geometry is taken as M2129 inlet duct. The Experimental data for M2129 intake is available in the literature<sup>3</sup> for a range of throat Mach numbers. Flow solutions and the adjoint based sensitivity derivatives are obtained with the open source SU<sup>2</sup> software.<sup>2</sup> For the optimization study, a single set of boundary conditions is employed for all the cases investigated. This single set of boundary conditions results in throat Mach number of 0.708, PR value of 0.968 and DC60 value of 0.483 for baseline geometry.

### II.A. Turbulent Flow and Adjoint Solver: SU<sup>2</sup>

Open source SU<sup>2</sup> software is developed for solving conservation equations on unstructured grids and one of the key feature of the SU<sup>2</sup> software is its ability to optimize aerodynamic shapes with adjoint-based methodologies. Adjoint based optimization methods originates from the control theory and the governing equations of the flow-field becomes a constraint so that the final expression for the gradient does not require reevaluation of the flow-field.<sup>4</sup> As a result the cost of the optimization process is reduced significantly especially for the optimization studies at which large number of design parameters are involved.

In this study steady RANS solver of SU<sup>2</sup> is used for turbulent flow solutions. In RANS solutions air is modeled as an ideal gas with the constant specific heat ratio of 1.4 and the gas constant taken as 287.058 J/kgK. In order to close the system of equations, SA turbulence model, which is based on Boussinesq hypothesis, is used for modeling turbulent viscosity and dynamic viscosity is obtained with classical Sutherland formulation.<sup>5</sup> The central Jameson-Schmidt-Turkel (JST) flux splitting method and the Green Gauss theorem for gradient calculations are employed. Venkatakrishnan slope limiter is used for limiting the gradients. The CFL number of 15 is kept constant for the RANS calculations. The discrete adjoint solver setting is kept consistent with the CFL reduction factor of 0.1.

In the adjoint based optimizations the RANS solution is first obtained using SU2\_CFD module. Then, SU2\_CFD\_AD module is utilized for adjoint solutions. For projecting the adjoint sensitivities on the design variables SU2\_DOT\_AD module is used. After multiplying the sensitivities with the relaxation factors, mesh deformation is performed in accordance with the FFD Box displacements within SU2\_DEF module. The steps are repeated until convergence criteria for the minimum gradient is reached. All these steps are driven by a single python script.

### II.B. Computational Domain

In numerical solutions M2129 intake is modeled without the intake lips and the center body which simulates the hub of the engine. M2129 intake is a circular cross section S-shaped duct with a diffusion ratio of 1.4. Centerline curvature and radius variation in axial direction are given in Equation 1 and Equation 2 respectively. In these equations  $Z$  shows vertical offset and  $X$  shows axial distance from the very first point of the S-duct.

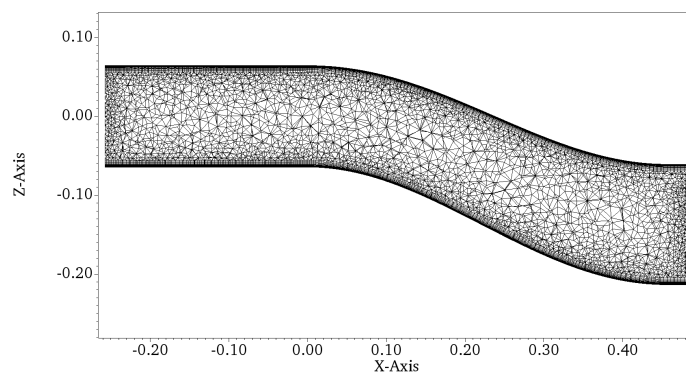


Figure 1: Mesh Distribution in Symmetry Plane

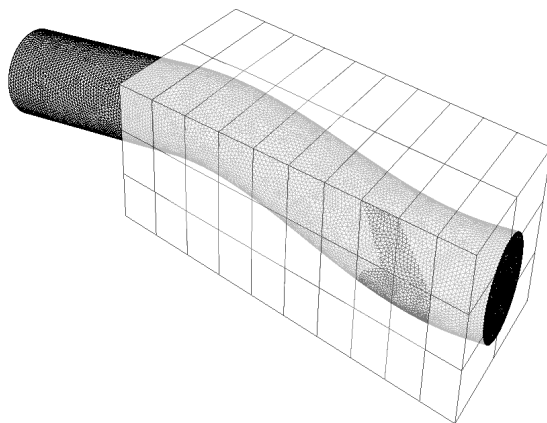


Figure 2: FFD Box Around Inlet Duct

$$Z_{cl} = \Delta Z [1 - \cos(\pi \frac{X_{cl}}{L})] \quad (1)$$

$$\frac{R - R_i}{R_{ef} - R_i} = 3(1 - \frac{X_{cl}}{L})^4 - 4(1 - \frac{X_{cl}}{L})^3 + 1 \quad (2)$$

Additionally, a length of 26.8cm constant cross section is added to the upstream of the duct to develop the boundary layer. In the earlier study conducted by Mohler,<sup>3</sup> same intake configuration is computationally investigated with and without vortex generators.

The computational mesh is composed of 1.4 million cells with 30 layers of boundary layer prisms.  $y^+$  value is kept below 1. Pressure inlet boundary condition is applied at the upstream boundary whereas pressure outlet boundary condition is applied at the aerodynamic interface plane (AIP). The duct walls are modeled as no-slip wall. The unstructured mesh on symmetry is shown in Figure 1.

A Free form deformation(FFD) box covers the inlet geometry to be modified. It starts from the throat area and ends at AIP. The FFD box is composed of 11 axial, 4 vertical and 3 horizontal planes. The first and the last planes of the free form deformation box are kept constant, so that the overall diffusion ratio and throat shape are not modified. Additionally, the vertical offset between the throat and the AIP is not allowed to change. A Bezier curve is used as a blending function and the first order slope continuity is

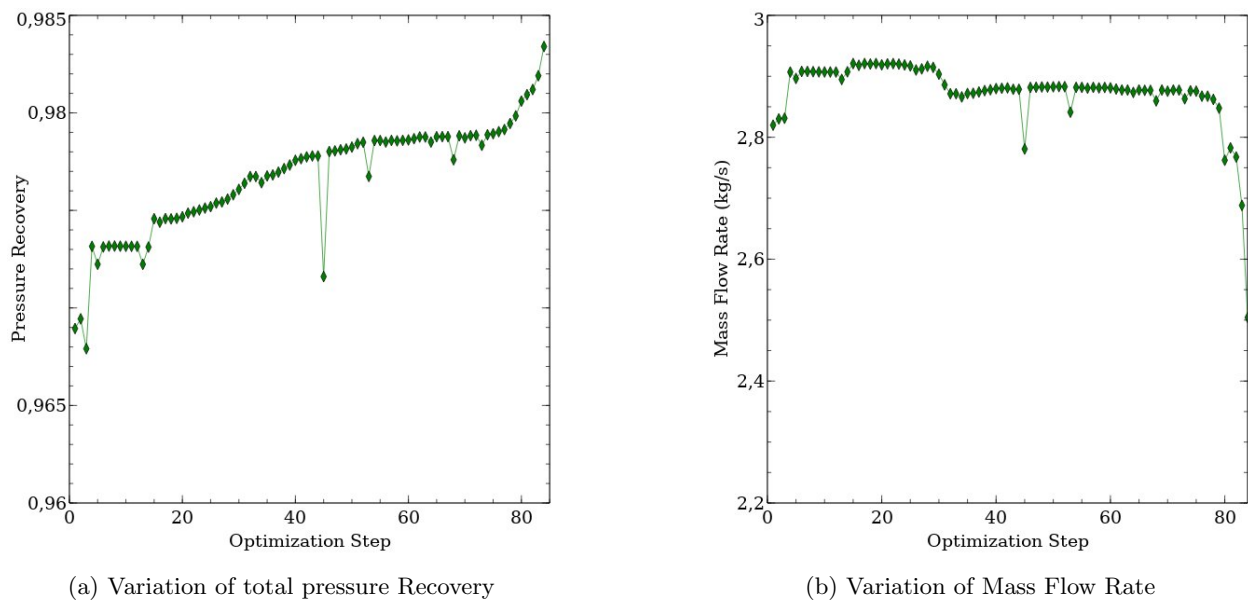


Figure 3: Variation of Total Pressure recovery and mass flow rate along optimization steps in Case 1

ensured by the SU2\_DEF module. The free form deformation box used in the optimization study is shown in Figure 2.

### III. Results and Discussion

In this study three optimization cases are considered. In the first case only the total pressure at AIP is maximized. In the second case the total pressure at AIP is maximized with a constraint on the minimum mass flow rate. In the last case, the mass flow rate is maximized with no constraints.

#### III.A. Case 1: Maximization of total pressure at AIP

The variation of the total pressure recovery at AIP and the mass flow rate along the optimization steps are given in Figures 3a and 3b. As observed the pressure recovery improves along the optimization steps, whereas the mass flow rate initially improves but at about 80th step, it drops rapidly. The optimization algorithm finds a direction in which the shape change results in maximizing the total pressure while decreasing the mass flow rate. The optimization process is therefore stopped at the 85th step.

The corresponding optimum duct shape is given in Figures 4 and 5. As seen, the optimization process results in a quite unconventional duct curvatures at the symmetry plane. The optimized duct now has a lower curvature at the first bend while it has a very aggressive curvature at the second bend. At the second bend, the lower part of the duct makes a bump-shape curvature. The duct cross section at 0.3 meter location (Figure 5c) flattens at the bottom before it matches the circular cross-section at the AIP.

The optimum flow parameters are compared to the baseline values in Table 1. It is noted that the optimization process results in a higher pressure recovery and lower distortion values, but the mass flow rate and the throat Mach number is reduced. These findings are further discussed in Section III.D.

Table 1: Performance Parameters in Case 1

	PR	DC60	MFR(kg/s)	Throat Mach
<b>Baseline</b>	0.968	0.483	2.819	0.708
<b>85th Optimization Step</b>	0.983	0.140	2.504	0.575

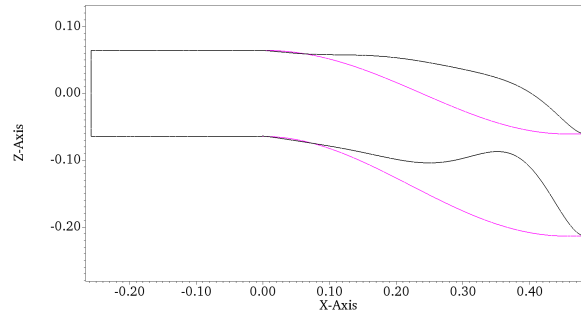


Figure 4: Duct Profiles at Symmetry Plane in Case 1 - Baseline (Pink) and Optimized (Black)

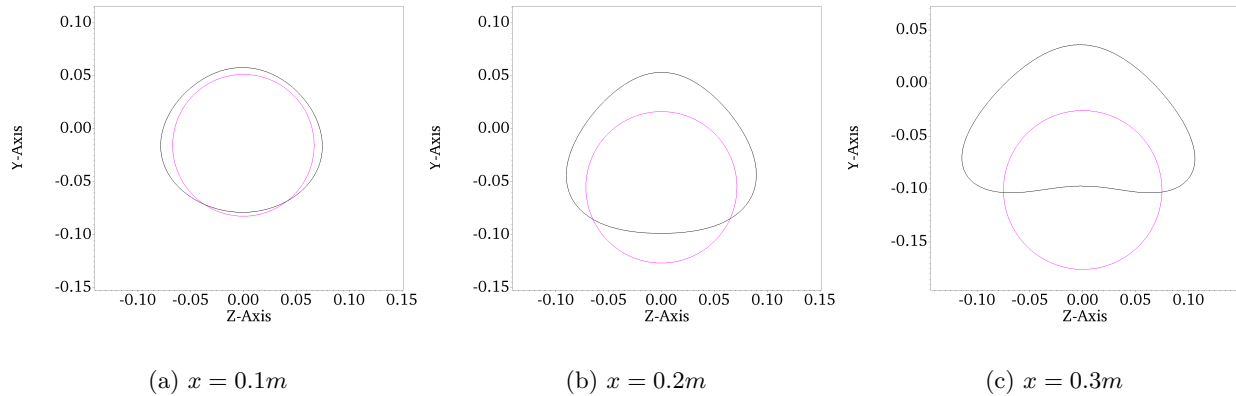


Figure 5: Duct Cross-Sections in Case 1 - Baseline (Pink) and Optimized (Black)

### III.B. Case 2: Maximization of total pressure at AIP with a Constraint on Mass Flow Rate

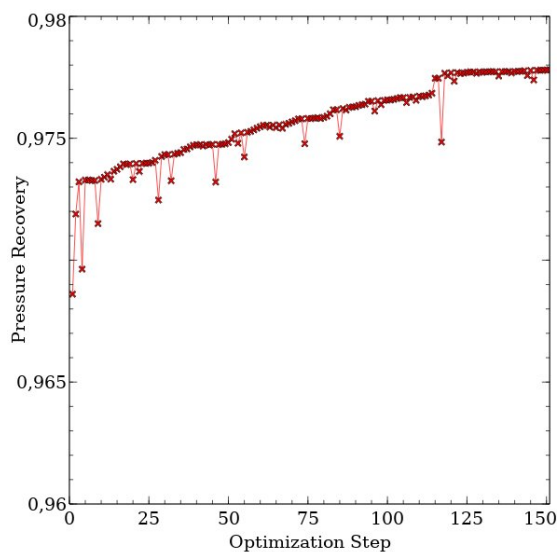
In order to prevent the rapid reduction in mass flow rate, in this optimization case the minimum mass flow rate is constrained at a 3% higher target value than that of the baseline. As shown in Figures 6a and 6b, the total pressure and the mass flow rate now increase along the optimization steps. However, as the mass flow rate approaches its target value, the pressure recovery converges to a value of 0.978, which is smaller than the ones observed in the previous case.

The optimum duct profile on the symmetry plane and the cross sections along the duct are given in Figures 7 and 8 respectively. It is observed that the shape deformations are smaller in comparison to the previous case. Yet, the same flattening of the duct cross-section at the bottom towards the AIP and the reduced profile curvature at the first bend are noticed.

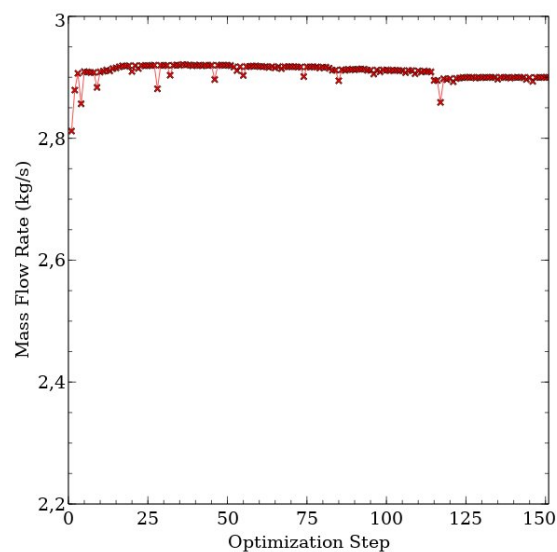
The performance parameters for the optimum duct shape are given in Table 2. It is concluded that in this constrained optimization case, the total pressure at the AIP may successfully be maximized while the mass flow rate requirement is satisfied.

Table 2: Performance Parameters in Case 2

	PR	DC60	MFR(kg/s)	Throat Mach
<b>Baseline</b>	0.968	0.483	2.819	0.708
<b>Optimized</b>	0.978	0.320	2.900	0.747



(a) Variation of total pressure Recovery



(b) Variation of mass flow rate

Figure 6: Variation of Total Pressure recovery and mass flow rate along optimization steps in Case 2

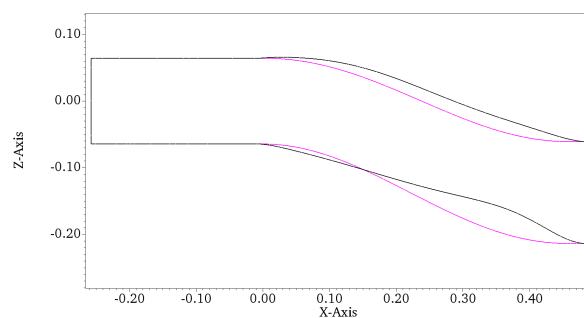
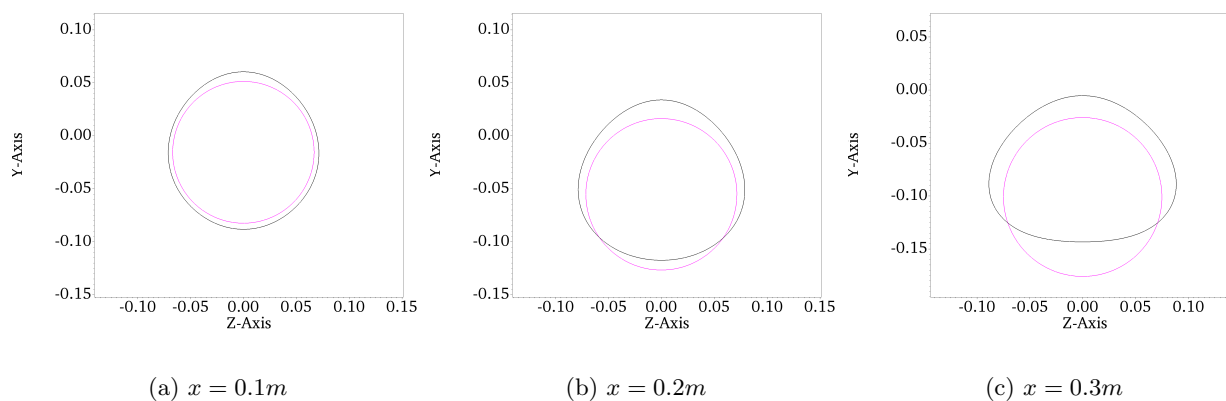


Figure 7: Duct Profiles at Symmetry Plane in Case 2 - Baseline (Pink) and Optimized (Black)

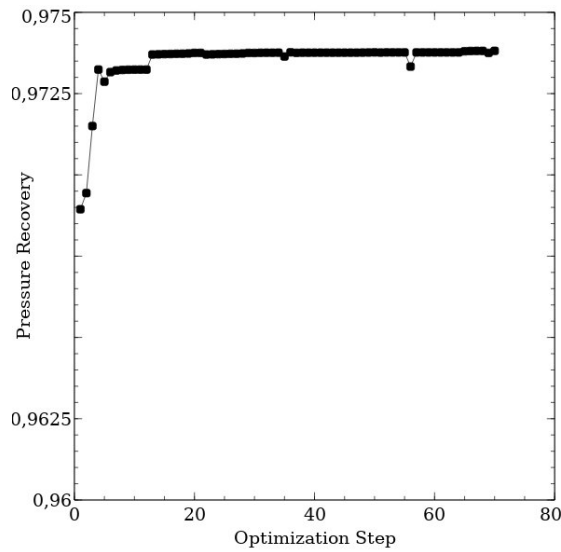


(a)  $x = 0.1m$

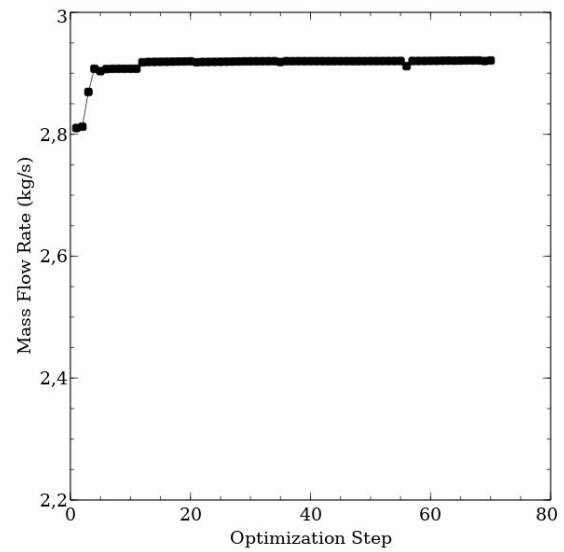
(b)  $x = 0.2m$

(c)  $x = 0.3m$

Figure 8: Duct Cross-Sections in Case 2 - Baseline (Pink) and Optimized (Black)



(a) Variation of total pressure Recovery



(b) Variation of mass flow rate

Figure 9: Variation of Total Pressure recovery and mass flow rate along optimization steps in Case 3

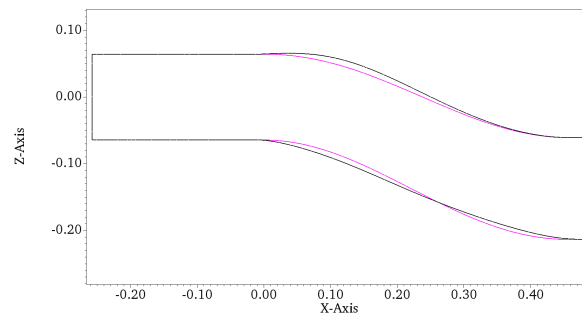
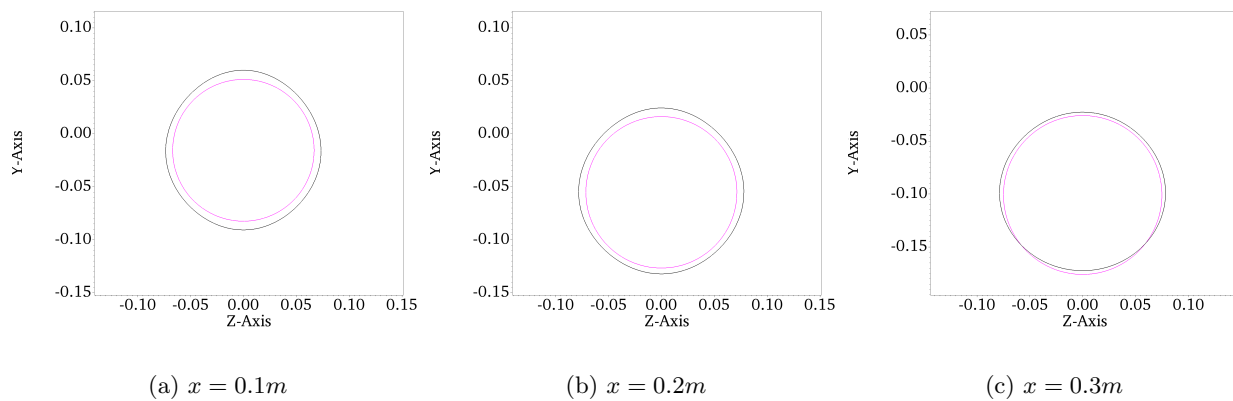


Figure 10: Duct Profiles at Symmetry Plane in Case 3 - Baseline (Pink) and Optimized (Black)



(a)  $x = 0.1m$

(b)  $x = 0.2m$

(c)  $x = 0.3m$

Figure 11: Duct Cross-Sections in Case 3 - Baseline (Pink) and Optimized (Black)

### III.C. Case 3: Maximization of Mass Flow Rate

Finally a single objective optimization is performed in order to maximize the mass flow rate without any constraint. The variations in pressure recovery and the mass flow rate along the optimization step are given in Figure 9. As expected as the mass flow rate increases, the pressure recovery improves in parallel. The optimum longitudinal profile and the duct cross-sections are similarly given in Figures 10 and 11. This time it is observed that the slope at the first bend increases slightly and the cross sections preserve their circular shape.

The performance parameters of the optimum duct shape are compared with the baseline values in Table 3. As expected, this single objective optimization provides the maximum mass flow rate among all the three cases and improves the pressure recovery at the expense of flow uniformity.

Table 3: Performance Parameters in Case 3

	PR	DC60	MFR(kg/s)	Throat Mach
<b>Baseline</b>	0.968	0.483	2.819	0.708
<b>Optimized</b>	0.974	0.398	2.921	0.765

### III.D. Further Assessment of Optimization Cases

In order to better understand the effects optimization objectives on the total pressure recovery and the mass flow rate, the geometrical properties of the optimum duct shapes and the flow characteristics inside the optimum ducts are further investigated.

Figure 12 shows the total pressure distributions on the symmetry plane and on the cross-sectional planes in the axial direction for all the optimum shapes obtained in the case studies together with the baseline geometry. It is observed that in order to reduce the total pressure losses the optimization process tends to flatten the bottom surface and increases the cross-sectional area. Such a geometrical modification is known as Gerlach shaping,<sup>6</sup> which minimizes the radial pressure gradients across the ducts with bends.

The static pressure distributions at the symmetry plane are given in Figure 13 for all the cases. It shows that the optimum shape obtained in Case 1 has a significantly higher static pressure distribution beyond the first bend. Such a pressure increase is attributed to the reduced flow speed due to the significantly increased cross-sectional area as shown in Figure 14. A similar trend is also observed in Case 2.

Pressure recovery and mass flow rate values obtained from the optimization studies are compared with the baseline intake performance in Table 4. As expected highest total pressure recovery is obtained from Case 1, in which a single objective is assigned as maximizing total pressure. However, the mass flow rate is significantly reduced in this case. This reduction in mass flow rate is originating from the high static pressure around the first bend. At the same time Case 3, which aims to maximize mass flow rate only, provides the highest mass flow rate among all three cases, and maximizing mass flow rate only results in 0.62% increase in total pressure recovery. In Case 2, the mass flow rate constraint is successfully satisfied and a significant increase in total pressure recovery is obtained.

Table 4: Performance Parameters

	PR	% Change	MFR(kg/s)	% Change
Baseline	0.968	-	2.819	-
Case 1	0.983	1.55	2.504	-11.17
Case 2	0.978	1.03	2.900	2.87
Case 3	0.974	0.62	2.921	3.62

## IV. Conclusion

In this study the M2129 intake duct is successfully optimized for the minimization of total pressure losses and maximization of the mass flow rate. The duct is represented within a free form deformation box with a total of 54 design variables. The adjoint based optimizations are performed using the open source



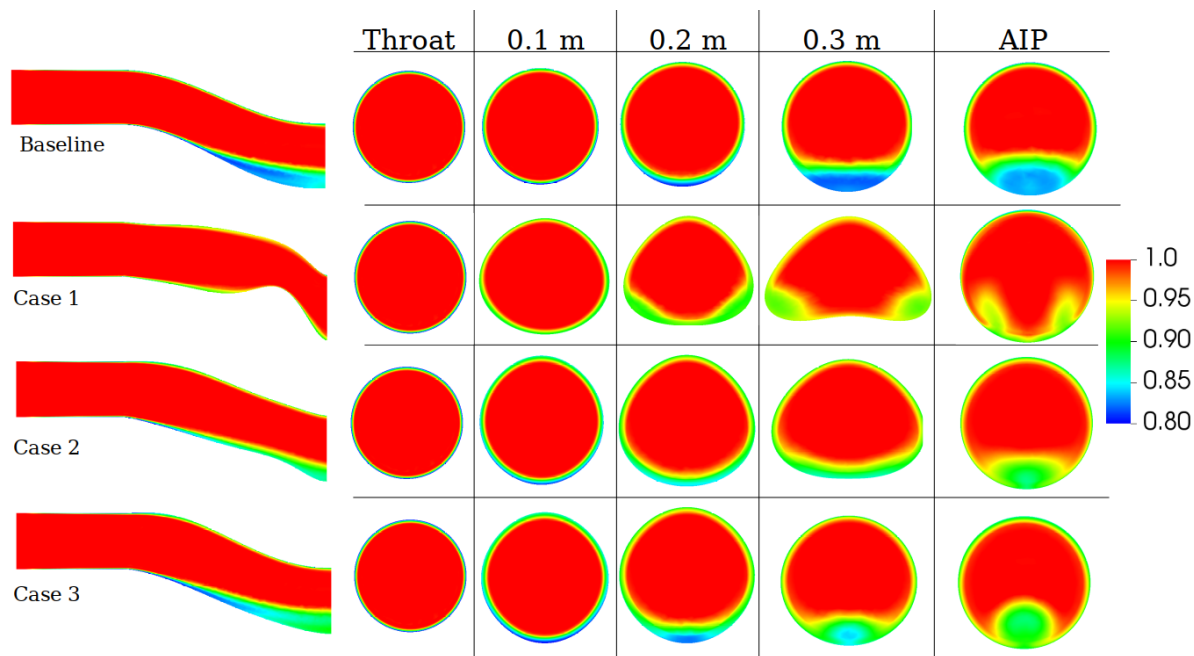


Figure 12: Sectional Pressure Recovery Distributions

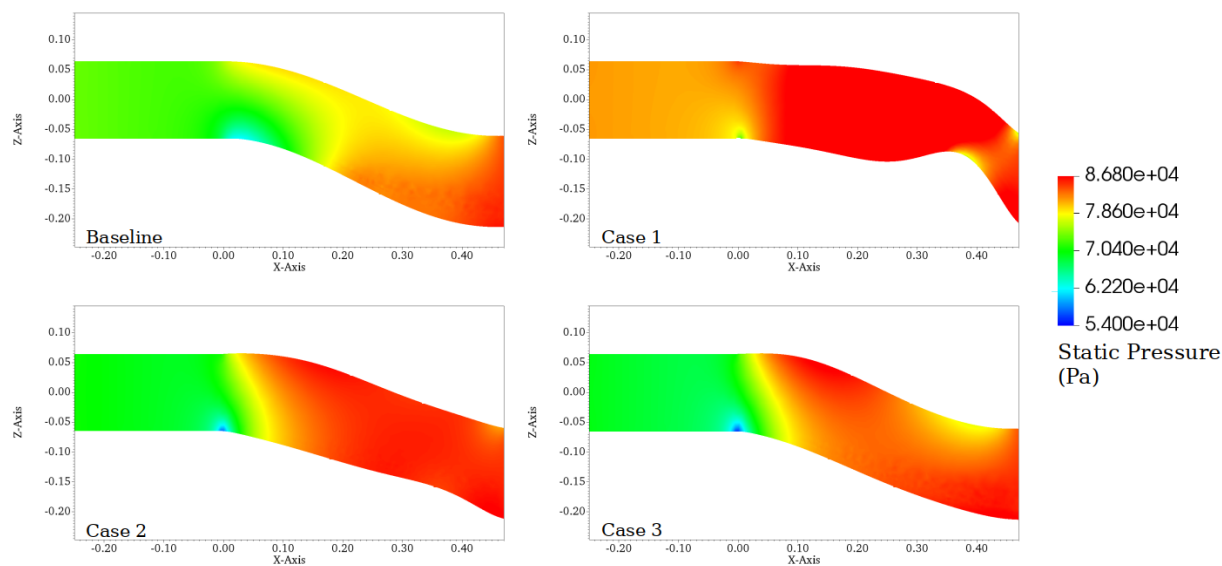


Figure 13: Sectional Pressure Distributions

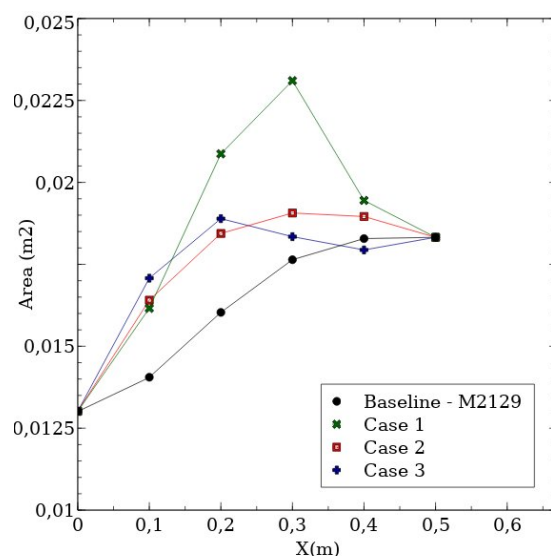


Figure 14: Variation of Cross Section Area in Axial Direction

CFD software SU<sup>2</sup> and its discrete adjoint module. Three optimization cases are performed with different set of objectives. The single objective optimization for the maximization of pressure recovery results in reduced mass flow rates. The optimizations with the constrained mass flow rate and the single objective optimization for the maximization of the mass flow rate improve the pressure recovery at AIP and the mass flow rate as much as 1.03% and 3.62%, respectively. It is concluded that inlet ducts can successfully be optimized with adjoint based methods to maximize the mass flow rate, which incidently maximizes the total pressure recovery. It is observed that the optimum duct shapes where the bottom surface following the first bend flattens out are similar to the well-known "Gerlach" shape. In addition, the cross sectional area inside the optimum duct shapes grows upstream of the AIP so that favorable pressure gradients are generated at the AIP.

## References

- <sup>1</sup>AGARD FTP Working Group 13, Air Intakes for High Speed Vehicles, AR270, Sept. 1991.
- <sup>2</sup>Thomas D. Economon, Francisco Palacios, Sean R. Copeland, W. Lukaczyk, and Juan J. Alonso. SU2:An Open-Source Suite for Multi physics Simulation and Design. AIAA Journal Vol. 54, No. 3, March 2016.
- <sup>3</sup>Mohler, Stanley. "Wind-US flow calculations for the M2129 S-duct using structured and unstructured grids." 42nd AIAA Aerospace Sciences Meeting and Exhibit. 2004.
- <sup>4</sup>Nadarajah, Siva, and Antony Jameson. "A comparison of the continuous and discrete adjoint approach to automatic aerodynamic optimization." 38th Aerospace Sciences Meeting and Exhibit. 2000.
- <sup>5</sup>F.M. White. Viscous Fluid Flow. McGraw Hill Inc., New York, 1974
- <sup>6</sup>C.R. Gerlach, E.C. Schroeder, Study of minimum pressure loss in high velocity duct systems. Technical Report No 1, Contract No. NAS8-21133 (NASA, 1969)